

Two-Tier Nanolaminate Plasmonic Crystals for Broadband Multiresonant Light Concentration with Spatial Mode Overlap

Seied Ali Safiabadi Tali, Junyeob Song, Wonil Nam, and Wei Zhou*

Effective trapping and nanolocalization of different colored photons simultaneously at the same position remain a challenge in nanophotonics research but can boost applications based on nonlinear multiphoton processes. For achieving broadband nanoscale light concentration, a promising strategy is to employ multiresonant plasmonic devices that support multiple hybridized surface plasmon modes with spatial overlap at several different resonance wavelengths. However, high-order plasmonic modes from hybridization tend to have a dark multipolar nature and are less useful due to weak interactions with free-space light. Here, it is reported that nanolaminate plasmonic crystals in a two-tier configuration can support many (≈ 10) spatially overlapped and highly-excitabile hybridized plasmonic modes under free-space light illumination between 400 and 1400 nm. Combination of nanoimprinting lithography and multilayered physical vapor deposition techniques enables wafer-scale fabrication of nanolaminate plasmonic crystals consisting of nanolaminate nanodome and nanohole arrays as the two closely-separated subsystems, and measurements demonstrate their multiresonant plasmonic responses in good agreement with numerical calculations. Coupled-mode theory analysis reveals that the unique broadband multiresonant responses of the two-tier nanolaminate plasmonic crystals are due to the synergistic effects of the strong near-field interactions between the modes in the nanodome and nanohole subsystems and the ground-plane-like loading effect from the nanohole subsystem.

scattering, photoluminescence, and electroluminescence.^[4–8] Nevertheless, for many nonlinear nanophotonics applications, it is highly desirable to use multiresonant plasmonic devices that can simultaneously enhance multiphoton excitation/emission processes in several different wavelength bands at the same hotspot locations.^[9–19]

For constructing multiresonant plasmonic devices, a general approach is to assemble multiple building-block plasmonic resonators within a very close distance; and the optical coupling between spectrally matched non-orthogonal elementary modes of building blocks can result in multiple hybrid plasmonic modes of different resonance wavelengths that spatially overlap.^[20–22] Based on the geometrical configuration of building-block resonators, multiresonant plasmonic devices can be classified into three types: 1) in-plane arrangement,^[9,11,12,15,18,23–27] 2) core-shell arrangement,^[14,28–32] and 3) out-of-plane arrangement.^[33–37] Since it is straightforward to create plasmonic systems with accurate nanoscale control of planar geometries by top-down nanolithography, most previous studies have focused on developing in-plane multiresonant plasmonic devices.^[9,11,12,15,18,23–27]

Despite the simplicity in design and fabrication, in-plane multiresonant plasmonic devices face two severe limitations due to the planar layout of multiple building-block resonators. 1) The device footprint tends to be large, and accordingly, the surface density of multiresonant hotspots is typically low; 2) Since the nearest-neighbor coupling of elementary modes dominates between in-plane arranged building-block resonators, the planar multiresonant systems usually support a limited number (< 4) of hybridized plasmonic modes with spatial overlaps. Recently, Reshef et al. demonstrated that using in-plane plasmonic metasurfaces with a finite out-of-plane dielectric cladding can increase the number of modes by creating several Fabry-Perot-like (FP-like) resonances.^[38] However, such a method primarily depends on the broad electric dipolar plasmonic modes, limiting the maximum attainable absorption to 50%^[39] and keeping the field enhancement factor relatively small compared to nanogap plasmonic modes.^[20] As the second type of multiresonant plasmonic devices, chemically synthesized core-shell metal-insulator-metal (MIM) multilayered nanoparticles can support multiple hybrid modes by mixing the elementary modes at

1. Introduction

Plasmonic nanostructures can serve as resonant optical nanoantennas to trap and concentrate light at the deep subwavelength scale and thus can enable nanolocalized enhancement of light-matter interactions for various applications in energy conversion, information technology, biochemical sensing, and spectroscopy.^[1–6] Conventional designs of plasmonic devices optimize single-resonant near-field characteristics within one wavelength band, which is sufficient for applications based on single-photon excitation/emission processes, including photothermal conversion, hot carrier generation, elastic/inelastic

S. A. Safiabadi Tali, Dr. J. Song, W. Nam, Dr. W. Zhou
Department of Electrical and Computer Engineering
Virginia Tech
Blacksburg, VA 24061, USA
E-mail: wzh@vt.edu

 The ORCID identification number(s) for the author(s) of this article can be found under <https://doi.org/10.1002/adom.202001908>.

DOI: 10.1002/adom.202001908

different metal-dielectric interfaces,^[14,28–32] but have difficulties in accurate nanoscale control of core-shell geometries for scalable fabrication. The third type of multiresonant plasmonic devices, i.e., out-of-plane MIM multilayered nanostructures, has recently drawn increasing attention.^[33–37] By allowing for vertical stacking of many MIM resonator building blocks with shared metal layers between the neighboring blocks, out-of-plane multiresonant plasmonic devices can have appealing features,^[35] including 1) increased surface density of multiresonant hotspots in plasmonic nanogaps, and 2) scalable fabrication by well-controlled thin-film deposition and nanolithography processes. Despite the substantial development of different multiresonant plasmonic devices, a crucial but challenging issue remains that high-order modes from plasmon hybridization tend to have a dark multipolar nature and interact poorly with free-space light.^[20,22]

Here, we report a new type of two-tier multiresonant plasmonic system—nanolaminate plasmonic crystals (Figure 1a)—that can support many (≈ 10) hybridized plasmonic modes with spatial overlap and can allow for multiresonant nanoscale light concentration across a wide wavelength range between

400 and 1400 nm. Uniquely, nanolaminate plasmonic crystals have a two-tier configuration and consist of two closely-separated multiresonant plasmonic subsystems, respectively, 1) a MIM nanolaminate nanodome array that supports multiple localized plasmonic modes M_n^L (Figure 1b), and 2) a MIM nanolaminate nanohole array that supports multiple delocalized plasmonic modes M_n^D (Figure 1c). As illustrated in Figure 1d, the coupled-mode theory (CMT) analysis reveals that the optical interactions between Mode A in the nanolaminate nanodome array (modeled as a side-coupled Resonator A) and Mode B in the nanolaminate nanohole array (modeled as a directly-coupled Resonator B) can significantly increase the total light absorption in the coupled system, much over the summed light absorption from the two subsystems. From the CMT analysis (details in the Supporting Information), we find that the absorption increase for the coupled system has two primary microscopic origins, including 1) the near-field mutual coupling between Mode A and Mode B, and 2) the ground plane-like loading effect of Resonator B, which enhances the coupling of Mode A to the incident light. Thus, through optical interactions between the two uncoupled multiresonant subsystems,

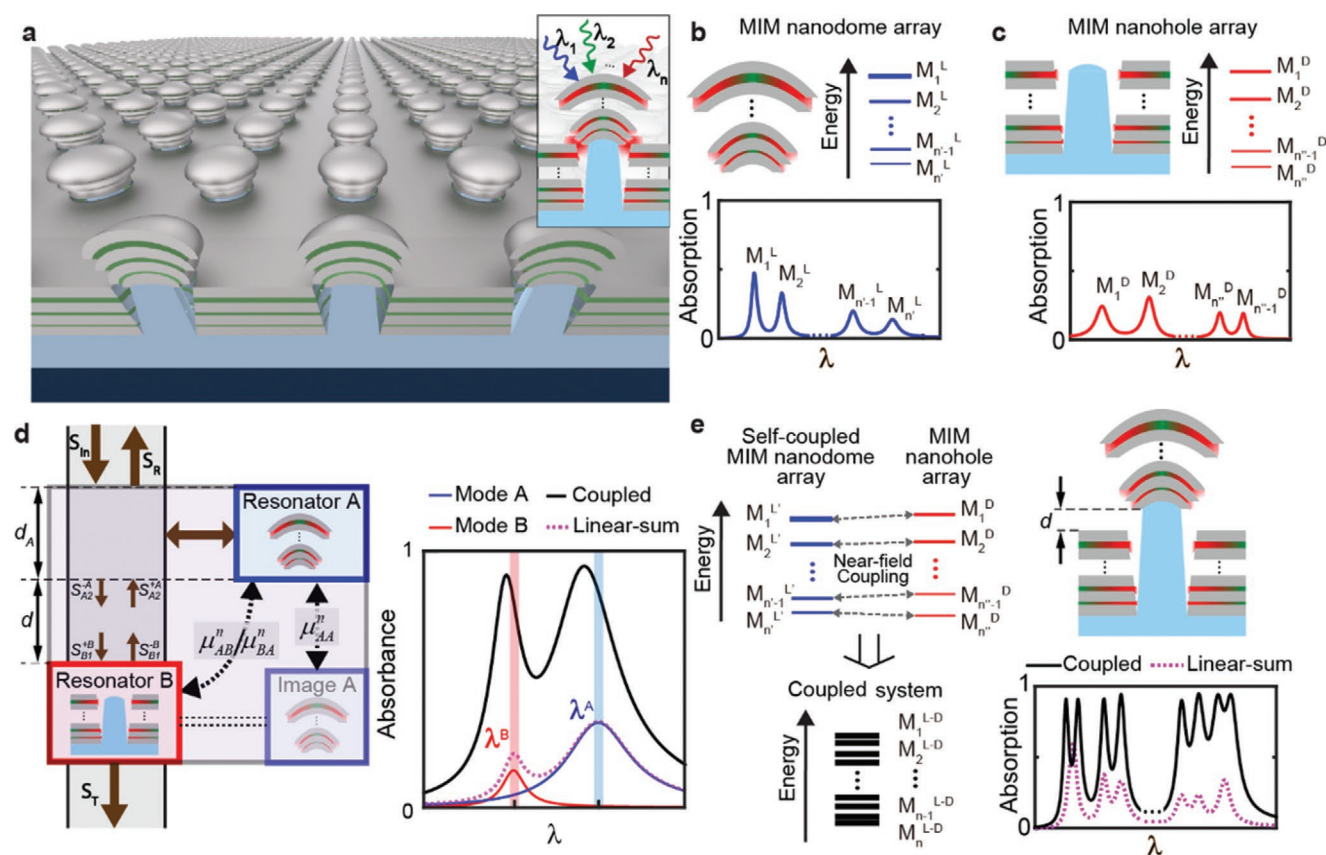


Figure 1. Nanolaminate plasmonic crystals in the two-tier configuration for broadband multiresonant nanolocalized light concentration. a) Scheme of nanolaminate plasmonic crystals consisting of nanolaminate nanodomains and nanohole arrays as the two multiresonant subsystems. b) Nanolaminate nanodomains support multiple localized plasmonic modes M_n^L by hybridization. c) Nanolaminate nanohole arrays support multiple delocalized plasmonic modes M_n^D by hybridization. However, the high-order modes from hybridization in multiresonant subsystems tend to have a dark multipolar nature. d) Coupled-mode theory (CMT) modeling and analysis of optical interactions between the representative Mode A and Mode B in the two subsystems, showing that the coupled system can have a higher light absorption than the summation of those from the two uncoupled subsystems. e) Schematic energy diagram and absorption spectra for the two-tier multiresonant systems that can support multiple hybrid plasmonic modes M_n^{L-D} with spatial overlaps and with stronger interactions with free-space light.

nanolaminate plasmonic crystals as the coupled two-tier multiresonant systems can support a series of hybrid $M_n^{L,D}$ modes, which have stronger interactions with free-space light compared to the uncoupled M_n^L and M_n^D modes (Figure 1e). Furthermore, compared to conventional in-plane multiresonant plasmonic systems, out-of-plane nanolaminate plasmonic crystals can possess a much higher surface density of hotspots for broadband multiresonant light concentration by a tight vertical stacking of many MIM nanocavities.

2. Results and Discussion

To validate the predictions from CMT analysis, we fabricated samples of nanolaminate plasmonic crystals in the two-tier configuration with different geometric designs and experimentally investigated their optical properties. Briefly, wafer-scale nanolaminate plasmonic crystals were created by line-of-sight electron beam evaporation of alternating Ag and SiO_2 layers on a nanoimprinted polymer nanopillar array.^[35] Such fabrication strategy can allow the self-alignment of the nanolaminate nanodomes above the nanolaminate nanoholes. Nanolaminate plasmonic crystals can show a very dark appearance in the top-view (Figure 2a), manifesting a broadband absorption in the visible range. Nevertheless, as viewed in an oblique angle (Figure 2b), we can observe a vivid rainbow-color due to the optical diffraction from periodic nanostructures on the sample. While the top-view scanning electron microscope (SEM) image (Figure 2c) shows a uniform periodicity for the nanostructures, the cross-sectional SEM image (Figure 2d) reveals irregular roughnesses and geometries at the surface of sidewalls for MIM nanodomes

and nanoholes. Also, the diameters of MIM nanodomes and nanoholes vary between individual units due to the geometry nonuniformity of nanowells in the PDMS template used for nanoimprinting the polymer nanopillar arrays. Notably, MIM nanodomes have an inversely tapered shape because of the shadowing effect in the line-of-sight electron-beam deposition.

As depicted in Figure 2e, we first investigated four different types of fabricated nanolaminate plasmonic crystals with 1 metal layer (1ML), 2 metal layers (2MLs), 3 metal layers (3MLs), and 4 metal layers (4MLs) by reflection and transmission spectroscopy (Figure 2f). Limited by the height of nanopillar arrays and the chosen thicknesses of individual metal/dielectric layers, the maximum total number of metal layers is four for our fabricated nanolaminate plasmonic crystals. The tapered shape of the nanodomes causes enlarged diameters of individual MIM nanocavities from the bottom to the top in the vertical stack, which leads to spectrally detuned elementary nanogap modes in MIM nanocavities of equal dielectric nanogap thicknesses.^[36] All the Ag layers have a fixed thickness of 30 nm. However, to allow spectral matching of elementary nanogap modes for effective hybridization, we have chosen increasing dielectric nanogap thicknesses from 5 nm in the bottom to 10 nm in the middle and 15 nm in the top for different individual MIM nanocavities. Notably, the symmetry breaking in the inversely tapered shape of MIM nanodomes can lead to a bianisotropic magneto-electric nature for the supported plasmonic nanogap modes.^[40] From reflection measurements (Figure 2f), 2MLs/3MLs/4MLs nanolaminate plasmonic crystals can support multiple resonant modes over a broad spectral range between 400 and 1700 nm. Furthermore, by stacking more metal-dielectric layers, the overall optical

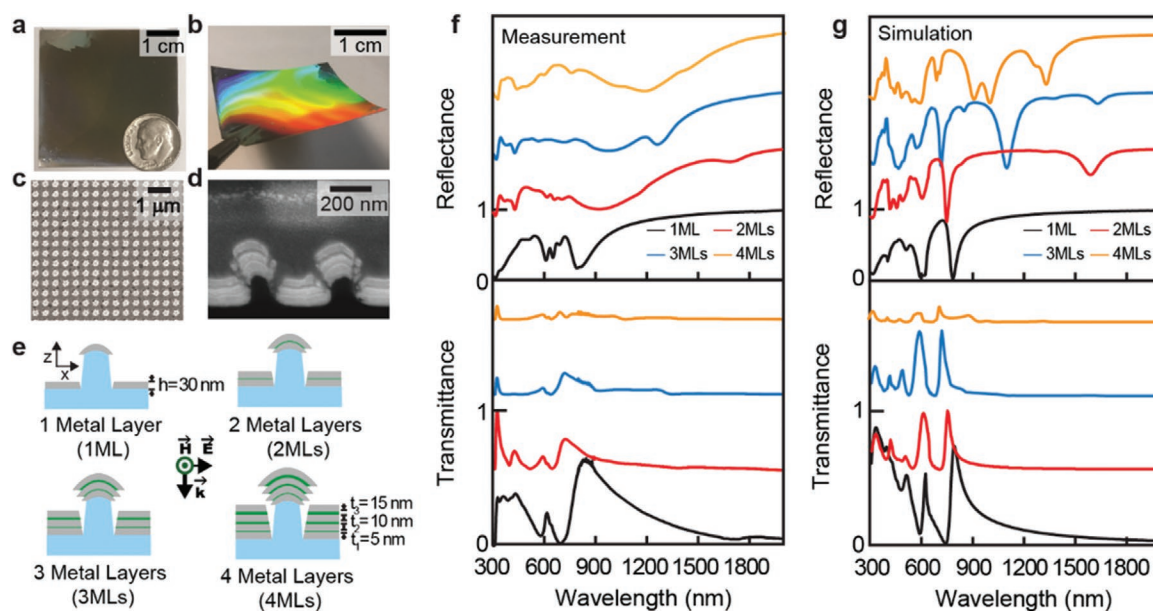


Figure 2. Multiresonant optical responses of fabricated nanolaminate plasmonic crystals with different numbers of metal-dielectric layers. a) Top-view and b) tilted-view optical camera images of a wafer-scale sample of the four-metal-layer nanolaminate plasmonic crystal. c) Top-view and d) cross-sectional scanning electron microscope (SEM) images of the 4MLs nanolaminate plasmonic crystal. e) Scheme of four different types of fabricated nanolaminate plasmonic crystals with 1 metal layer (1ML), 2 metal layers (2MLs), 3 metal layers (3MLs), and 4 metal layers (4MLs). The thicknesses of dielectric nanogap layers for nanolaminate plasmonic crystals increase from 8 nm in the bottom to 10 nm in the middle and 15 nm in the top, respectively. f) Measured and g) FDTD-calculated reflection and transmission spectra for the different samples of nanolaminate plasmonic crystals in (e).

response of nanolaminate plasmonic crystals can be changed significantly due to the introduction of some new modes and the spectral detuning of some existing modes. For example, the change from 1ML to 2MLs can cause a new mode emerging at ≈ 1650 nm, and a further change from 2MLs to 3MLs can spectrally shift this mode to ≈ 1300 nm. Transmittance measurements in Figure 2f reveal that only a subset of modes in reflection spectra can induce high optical transmission peaks, and the resonant wavelengths of these high-transmission modes (e.g., at 600–615 nm, and 750–850 nm) show relatively weak dependence on the geometric changes by adding more metal-dielectric layers in the system. To study the observed resonant features in measurements, we used the finite-difference time-domain (FDTD) simulations to calculate far-field and near-field optical properties of nanolaminated plasmonic crystals (see Experimental Section). In Figure 2g, the FDTD-calculated reflection and transmission spectra show different multiresonant optical responses among 1ML/2MLs/3MLs/4MLs samples, in agreement with experimental results. By comparing FDTD-calculated near-field profiles of modes in different samples, it is revealed that the added metal-dielectric interfaces in MIM nanodomains and nanohole arrays can introduce new localized and delocalized plasmonic modes into the system, which can also spectrally detune the existing plasmonic modes through near-field interactions. Furthermore, the transmission peaks are associated with Bloch SPP modes at the metal-substrate interface of MIM nanohole arrays.^[41] Compared to calculations, resonant features in the measurements show much broader linewidths, which can come from homogeneous broadening due to interface roughness and material defects/impurity and inhomogeneous broadening due to geometric variations between unit cells (Figure 2d). The differences in resonance wavelengths between measurements and simulations (Figure 2f,g) can originate from the deviations of geometric parameters and material optical constants in numerical simulations from the actual samples.

Unlike conventional in-plane engineered plasmonic systems, the multiresonant optical properties of nanolaminate plasmonic crystals also strongly depend on out-of-plane geometries, such as the thicknesses of individual dielectric nanogap layers. To investigate the effects of nanogap thickness t on the supported plasmonic modes, we fabricated 2MLs nanolaminate plasmonic crystals with different t ranging from 5 to 40 nm and measured their reflection (Figure 3a) and transmission spectra (Figure S1a, Supporting Information). As t increases from 5 to 40 nm, the resonant feature at 1600 nm blueshifts toward ≈ 900 nm. As t increases from 5 to 10 nm, a new resonant feature emerges at 1650 nm, which continuously blueshifts toward ≈ 1150 nm with t increasing from 10 to 40 nm. Furthermore, the modes associated with transmission peaks only negligibly shift. The FDTD calculations in Figure 3b and Figure S1b (Supporting Information) show similar t -dependence trends for different plasmonic modes supported in 2MLs plasmonic crystals in a decent match with the measurements in Figure 3a and Figure S1a (Supporting Information).

To understand the microscopic natures of different plasmonic modes in 2MLs nanolaminate plasmonic crystals as well as the origins behind their different t -dependent behaviors, we calculated the optical responses of the 2MLs nanolaminate

nanodome (Figure 3c) and nanohole arrays (Figure 3d) as the two uncoupled subsystems to compare with those of the coupled system (Figure 3e). As shown in Figure 3c, MIM nanodomains support two prominent absorption peaks associated with the superradiant electric dipole (ED) mode at $\lambda_1^L = 575$ nm,^[20,36] and the darker magnetic dipole (MD) gap mode at $\lambda_2^L = 1045$ nm^[20,36,42] (Figure S2, Supporting Information). Interestingly, the non-symmetric shape of the tapered nanodomains makes the ED mode at λ_1^L non-orthogonal to the gap plasmonic modes. Consequently, the dark high-order gap plasmonic modes^[20,40] can indirectly get excited through coupling to the ED mode, as exhibited by the several small peaks around $\lambda_1^L = 575$ nm in Figure 3c. Furthermore, the MD mode at λ_2^L becomes bianisotropic^[40] to achieve a larger optical absorption under the upward illumination than the downward illumination (Figure S2, Supporting Information). Figure 3d shows that the MIM nanohole array can induce multiple absorbance peaks by exciting the band-edge Bloch SPP modes of different lattice orders (details in Figure S3 in the Supporting Information). By 2D Fourier analysis of E_z field patterns for different gaps or interfaces, we can determine the dominant Bloch SPP modes responsible for a specific absorbance peak: 1) $\lambda_1^D = 400$ and $\lambda_2^D = 495$ are dominated by $(\pm 1, \pm 1)$ and $(\pm 1, 0)$ Bloch SPP modes at the metal-medium interface, respectively; 2) $\lambda_3^D = 585$, $\lambda_4^D = 730$, $\lambda_5^D = 970$, and $\lambda_6^D = 1385$ are associated with $(\pm 2, \pm 1)$, $(\pm 2, 0)$, $(\pm 1, \pm 1)$, and $(\pm 1, 0)$ Bloch SPP modes inside the dielectric layer of MIM nanohole array, respectively; 3) The supported resonant features at λ_1^D , λ_2^D , λ_3^D , and λ_4^D can also induce high transmission peaks due to the excitation of Bloch SPP modes at the metal-substrate interface (Figure S3, Supporting Information).

As shown in Figure 3e, 2MLs nanolaminate plasmonic crystals support multiple absorption peaks, and their peak wavelengths are close to but not the same as the modes in the uncoupled subsystems of MIM nanodomains (Figure 3c) and MIM nanohole arrays (Figure 3d). Indeed, the near-field interactions of elementary modes in uncoupled subsystems cause the observed spectral shifts of the hybrid modes in the coupled system of nanolaminate plasmonic crystals. FDTD-calculations of near-field mode profiles confirm that the modes in 2MLs nanolaminate plasmonic crystals (Figure 3g–k) share spatially correlated patterns with their associated dominant elementary modes in the uncoupled subsystems (more details in Figure S4 in the Supporting Information). For example, the hybrid modes at λ_1 , λ_2 , λ_3 in the 2MLs nanolaminate plasmonic crystal carry the near-field distribution features of both localized elementary modes at λ_1^L in the MIM nanodome array and delocalized elementary modes at λ_1^D , λ_2^D , and λ_4^D in the MIM nanohole array. Moreover, the hybrid modes at λ_4 and λ_5 in the 2MLs nanolaminate plasmonic crystal directly originate from the optical coupling between λ_2^L mode in the MIM nanodome array and λ_5^D and λ_6^D in the MIM nanohole array. As revealed by the FDTD-calculated absorption spectra in Figure 3c,d, the coupling between the subarrays can significantly increase the absorption of the modes at λ_1 , λ_3 , and λ_4 in the 2MLs nanolaminate plasmonic crystal. According to the CMT analysis, the increased absorption of these hybrid modes is due to the near-field interactions between spectrally overlapped modes in the uncoupled arrays as well as the ground plane-like loading

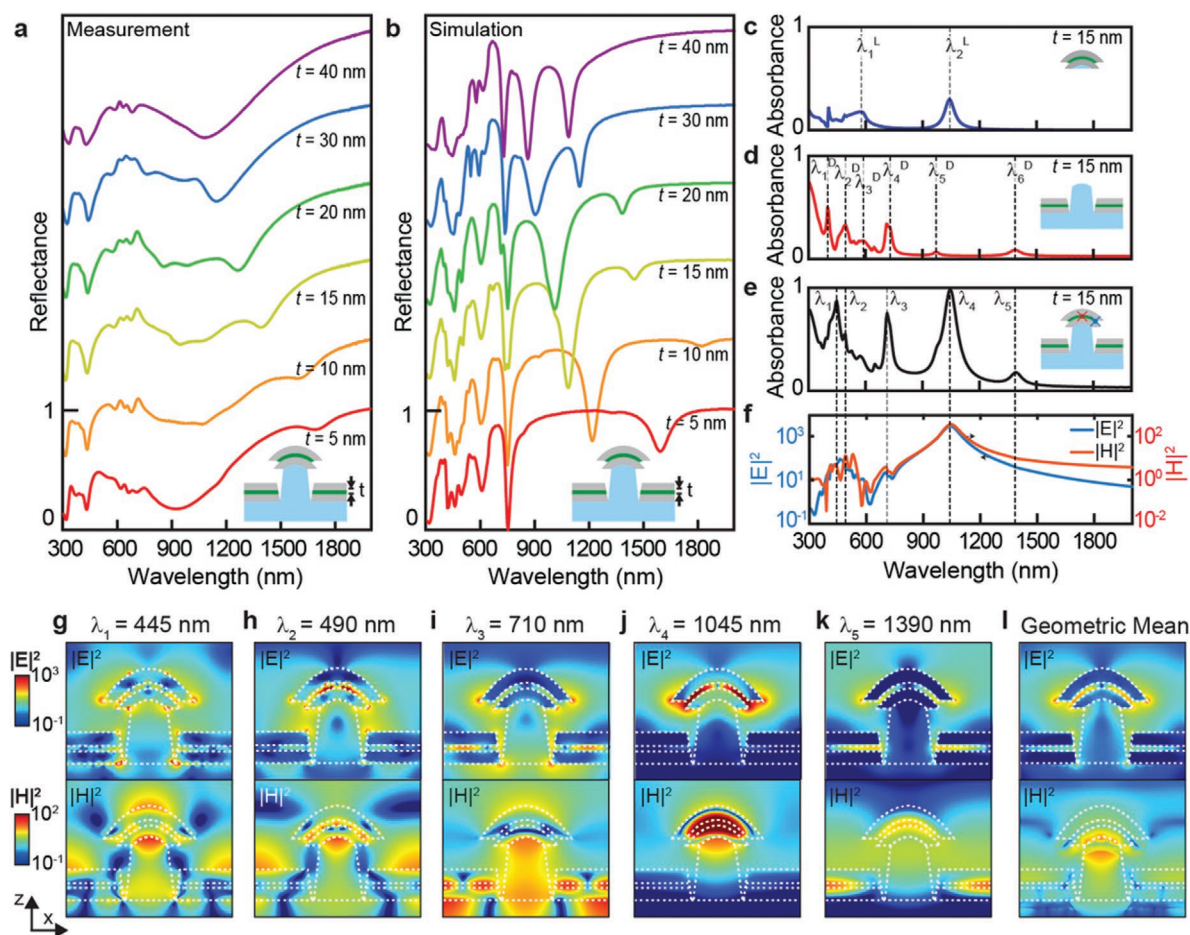


Figure 3. The strong dependence of multiresonant optical responses on the dielectric nanogap thickness (t). a) Measured and b) FDTD-calculated reflection spectra for 2MLs nanolaminate plasmonic crystals with different t from 5 to 40 nm. c, d) FDTD-calculated absorption spectra for the c) 2MLs nanolaminate nanodome and the d) 2MLs nanolaminate nanohole arrays as the two multiresonant plasmonic subsystems ($t = 15$ nm). e, f) FDTD-calculated spectra of e) absorption and f) near-field $|E|^2/|H|^2$ intensities for 2MLs nanolaminate plasmonic crystals with $t = 15$ nm. g–k) The FDTD-calculated x – z distribution maps of $|E|^2$ and $|H|^2$ for the modes λ_1 – λ_5 marked in (e). l) Geometrically-averaged x – z distribution maps of $|E|^2$ and $|H|^2$ among λ_1 – λ_5 modes.

effect from the nanohole array (details in the Supporting Information). FDTD-calculated near-field spectra (Figure 3f) and mode profiles (Figures 3g–l) demonstrate that 2MLs nanolaminate plasmonic crystals can induce $\approx 2/\approx 1$ order of magnitude enhancement of electric/magnetic field intensities widely between 400 and 1100 nm by supporting multiple plasmonic modes with spatial overlaps. Despite their promising multiresonant properties with spatial mode overlaps, the 2MLs nanolaminate plasmonic crystal still faces limitations of relatively low absorption in the wavelength range above 1100 nm.

As shown in Figure 2, the multiresonant optical responses of nanolaminate plasmonic crystals can be further improved by stacking more metal-dielectric layers as they introduce more elementary modes in the subsystems of MIM nanodomains and nanohole arrays. **Figure 4** provides a systematic analysis of the FDTD-calculated far-field and near-field optical properties for the different plasmonic modes supported in 4MLs nanolaminate plasmonic crystal. By comparing the absorbance spectra of the two uncoupled subsystems, 4MLs nanolaminate nanodome and nanohole arrays (Figure 4a,b), with the coupled 4MLs system

(Figure 4c), shows a spectral correspondence between resonance wavelengths of the modes in the coupled system and those in the uncoupled subsystems. Compared to the 2MLs MIM nanodome array (Figure 3c), the 4MLs nanolaminate nanodome array (Figure 4a) can support more plasmonic modes due to an increased number of metal-dielectric interfaces and accordingly supported localized plasmonic modes (Figure S5, Supporting Information), which contributes to the improved and broader multiresonant optical properties of the coupled 4MLs nanolaminate plasmonic crystal. Notably, in 4MLs nanolaminate nanodomains, $\lambda_1^L = 470$ nm, $\lambda_2^L = 495$ nm, and $\lambda_3^L = 595$ nm correspond to high-order nanogap modes, $\lambda_4^L = 1015$ nm is for the MD mode, and $\lambda_5^L = 1265$ nm and $\lambda_6^L = 1410$ nm correspond to subradiant magnetic modes of quadrupolar and octupolar natures, respectively. Similar to 2MLs nanodomains, the nanogap modes in 4MLs nanodomains are coupled to the ED mode, making them bianisotropic (Figure S5, Supporting Information). Furthermore, just as the 2MLs nanolaminate nanohole array, 4MLs nanolaminate nanohole array can support multiple Bloch SPP modes at different gaps and interfaces (Figure S6, Supporting Information).

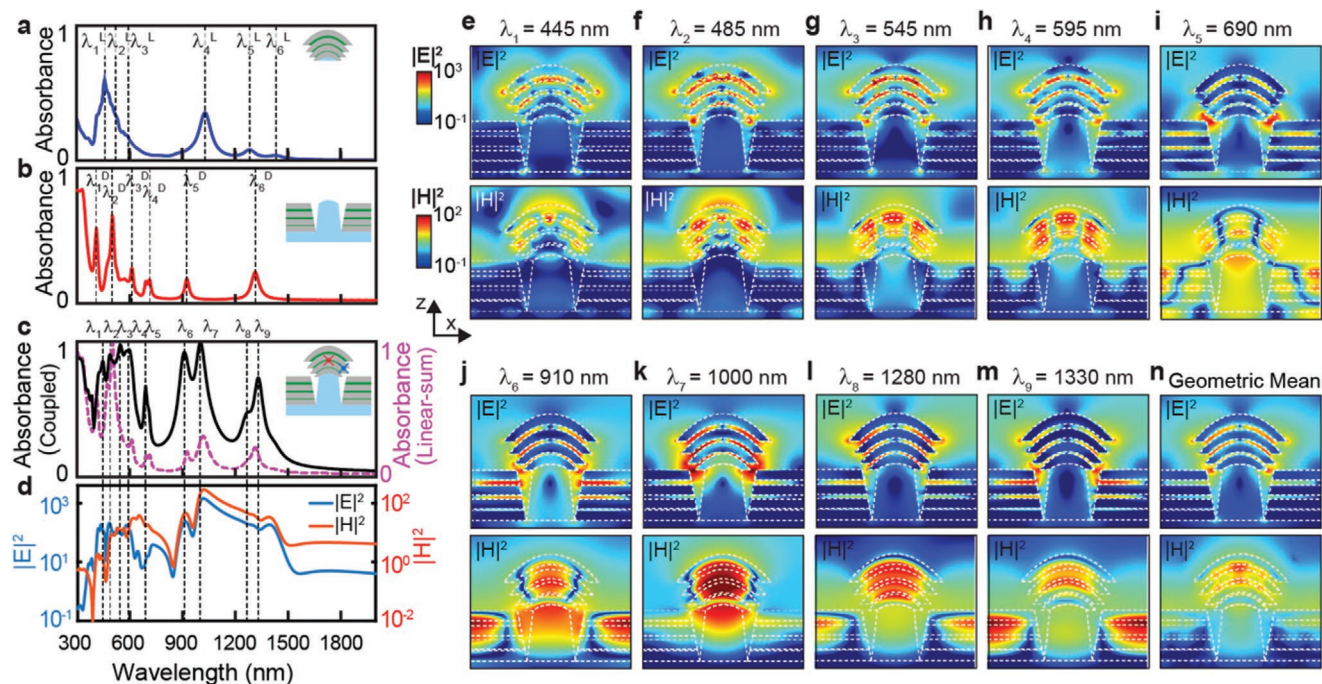


Figure 4. Broadband multi-resonant light concentration in dense arrays of nanogap hotspots. a,b) FDTD-calculated absorption spectra for a) 4MLs nanolaminate nanodome and b) 4MLs nanolaminate nanohole arrays as the two multi-resonant plasmonic subsystems. c,d) FDTD-calculated spectra of c) absorption and d) near-field $|E|^2/|H|^2$ intensities for the 4MLs nanolaminate plasmonic crystal. e–m) FDTD-calculated x – z distribution maps of $|E|^2$ and $|H|^2$ for the modes λ_1 – λ_9 marked in (c). n) Geometrically averaged x – z distribution maps of $|E|^2$ and $|H|^2$ among λ_1 – λ_9 modes.

Figure 4c shows that 4MLs nanolaminate plasmonic crystals can achieve much higher absorption than the summation of light absorption from the two uncoupled subsystems, i.e., 4MLs nanolaminate nanodome and nanohole arrays. From the FDTD-calculated near-field profiles of $|E|^2/|H|^2$ (Figure 4e–m), each mode in the 4MLs nanolaminate plasmonic crystal can be traced back to one or two elementary modes in the uncoupled 4MLs subsystems, and their near-field features are closer to the elementary mode with the higher spectral overlap (More details in Figure S7 and Table S1 in the Supporting Information). For example, the modes at $\lambda_1 = 445$ nm, $\lambda_2 = 485$ nm, and $\lambda_3 = 545$ nm mostly derive from the multiple high-order nanogap modes in the 4MLs nanodome array. The modes at $\lambda_4 = 595$ nm and $\lambda_5 = 690$ nm mainly originate from the delocalized Bloch SPP modes in the 4MLs nanohole array. Nevertheless, the modes at $\lambda_6 = 910$ nm, $\lambda_7 = 1000$ nm, $\lambda_8 = 1280$ nm, and $\lambda_9 = 1330$ nm have a mixed nature from the hybridization of both LSP modes in the 4MLs nanodome array and delocalized Bloch SPP modes in the 4MLs nanohole array. In addition to improved far-field broadband absorption, the 4MLs nanolaminate plasmonic crystal also shows an enhanced broadband near-field performance for subwavelength light concentration. As shown in Figure 4e–m, highly intense electric and magnetic fields can be concentrated in nanogap hotspots at nine different resonant wavelengths ranging from 400 to 1330 nm. The near-field distribution maps of geometrically-averaged field intensities at the nine different resonant wavelengths (λ_1 – λ_9) confirm the spatial overlap among all the modes with ≈ 3 and ≈ 2 orders of average magnitude enhancements for $|E|^2$ and $|H|^2$, respectively (Figure 4n), which agrees with the calculated spectra

of enhancement factors for $|E|^2$ and $|H|^2$ at nanogap regions (Figure 4d).

To investigate the effects of near-field interactions on multi-resonant optical properties, we calculated the absorption spectra of 4MLs nanolaminate plasmonic crystals at varying distances (d : 0 – 160 nm) between the top of the nanolaminate nanohole array and the bottom of the nanolaminate nanodome array (Figure 5a). As expected, all the modes in the 4MLs nanolaminate plasmonic crystal reach their highest absorbance levels at $d = 0$ nm, which from the CMT analysis (details in the Supporting Information) is due to the two synergistic effects: 1) Strong near-field interactions between elementary modes in the two subsystems; 2) Magnetic dipole natures of the gap LSP modes in tapered nanolaminate nanodomains can allow for enhanced absorption of light due to the constructive interference between the directly incident light and the back-reflected light from the ground-plane-like nanohole array subsystem. As d increases continuously from 0 to 160 nm, the overall absorption of different modes is reduced but with very different trends. The different d -dependence for different modes indicates that 1) there are different pathways for optical interactions between the subsystems, and 2) the relative contributions of different pathways depend on d and can be different for different modes. As shown in Figure 5b, the CMT-modeled d -dependent absorption curves (dashed curves) for the two representative modes λ^A and λ^B are in good agreement with FDTD calculations (solid dots). As a mode dominated by the elementary delocalized plasmonic Bloch modes in the nanolaminate nanohole array, λ^A mode shows a slightly increased absorption as d increases from 0 to 20 nm. As d further increases from 20 to 160 nm, the absorption

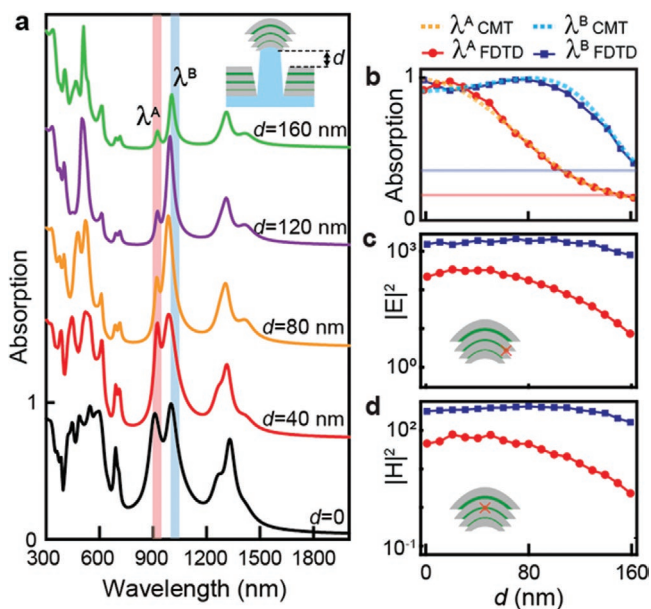


Figure 5. The strong dependence of multiresonant optical responses on the separation distance (d) between the two multiresonant subsystems. a) FDTD-calculated absorption spectra for the 4MLs nanolaminate plasmonic crystal with different d between 0 and 160 nm. b) Peak absorption values for λ^A and λ^B modes (also labeled in (a)) by FDTD calculations (solid curves & dots) and CMT modeling (dashed lines) as a function of d . Horizontal lines represent the absorption values for the corresponding modes in the uncoupled multiresonant subsystems. c, d) FDTD-calculated near-field intensities of c) $|E|^2$ and d) $|H|^2$ at resonant wavelengths for λ^A and λ^B modes as a function of d .

gradually decreases to a value slightly less than that of the uncoupled nanohole array. By comparison, as a mode dominated by the elementary localized mode in the nanolaminated nanodomains, λ^B mode shows reduced absorption as d increases from 0 to 20 nm. As d further increases from 20 to 80 and 160 nm, the absorption of λ^B mode first slightly increases and then reduces to a value slightly above that of the uncoupled nanodome array.

According to the CMT analysis (details in the Supporting Information), the decline of absorption for λ^A mode is due to the exponential weakening of its near-field coupling to λ^B mode. This weakening leads to an initial increase in λ^B absorbance as the energy transfer rate to the dark λ^A mode goes down. However, the increase of d also reduces the effective coupling of λ^B mode to the incident light due to the decreased degree of constructive interference between the direct and back-scattering coupling pathways, leading to the reduction of absorbance for λ^B mode. As shown in Figure 5c,d, the d -dependence curves of near-field $|E|^2/|H|^2$ intensities for λ^A and λ^B modes at nanogap hotspots have similar trends as their corresponding d -dependence far-field absorption curves, manifesting the correlated microscopic physics between the absorption from hot-carrier generation and the near-field enhancement from plasmonic charge/current accumulations in metal nanostructures. Overall, both FDTD simulations and CMT analysis indicate that a small distance between multiresonant subsystems is crucial to enhance the levels of absorption and local field concentration for all the modes in the two-tier multiresonant systems.

3. Conclusion

In conclusion, the nanolaminate plasmonic crystals in a two-tier configuration can support many spatially overlapped and highly excitable hybridized plasmonic modes to enable multiresonant nanoscale light concentration across a wide wavelength range of 400–1400 nm. From coupled-mode theory analysis and numerical simulations, the microscopic origin of highly excitable spatially overlapped multiresonant behaviors for the two-tier nanolaminate plasmonic crystals is due to the near-field coupling between the modes of the less excitable multiresonant subsystems as well as the ground-plane-like loading effect from the nanohole array subsystem. We envision that nanolaminate plasmonic crystals can serve as a high-performance multiresonant nano-optics platform to enhance multiple excitation/emission transitions of multiphoton nonlinear optical processes across a wide wavelength range simultaneously. By incorporating different functional materials (e.g., nonlinear materials, emissive gain medium, and strongly-correlated electronic materials) within different dielectric layers of nanolaminate plasmonic crystals, multifunctional active plasmonic devices can potentially be created with wavelength-multiplexed multiresonant capability.

4. Experimental Section

Sample Fabrication and Characterization: Nanolaminate plasmonic crystals were fabricated in cm^2 areas on flexible and heat-stabilized polyester (PET) films using nanoimprint lithography and directional electron beam deposition techniques. First, pre-patterned silicon (Si) wafer was used to create polydimethylsiloxane (PDMS) stamps with a periodic nanohole array with a height of 150 nm, a radius of 120 nm, and a periodicity of 400 nm, respectively. We then used the as-prepared PDMS stamp to squeeze one or two droplets of NOA83H optical adhesive (from Norland, USA) onto PET films. Next, the samples were cured by ultra-violet exposure (365 nm, 100 W) for 1 minute, detaching the PDMS stamp, and baking in a convection oven with 80 °C overnight. Finally, alternating layers of Ag and SiO_2 layers were deposited using an electron beam evaporator. A thin Cr adhesion layer (0.5 nm thickness) was deposited between alternating Ag and SiO_2 layers.

Far-Field Optical Measurements: Reflection and transmission far-field optical measurements were conducted using Cary 5000 UV-Vis-NIR spectrophotometer (Agilent Inc.).

Numerical Calculations: We performed 3D Finite Difference Time Domain simulations using commercial software (FDTD solutions, Ansys-Lumerical Inc.) to numerically calculate the far-field spectra and the near-field distributions of the plasmonic crystal systems and their building block arrays. A uniform mesh size of 3 nm (in x , y , and z directions) was used. The silver dielectric function was obtained from the Palik handbook of optical constants for solids.^[43] Also, the constant refractive index of 1.5 was used for SiO_2 .

Theoretical Modeling: Coupled-mode theory modeling and analysis were carried out to understand optical behaviors of nanolaminate plasmonic crystals. In this model, the two building-blocks of nanodome and nanohole arrays were treated as a side-coupled resonator and a directly-coupled resonator, respectively. The parameters of the uncoupled resonators in this model were obtained from FDTD simulations of the uncoupled nanodome and nanohole arrays. Furthermore, the near-field coupling parameters between the building-block arrays were obtained from the FDTD simulations of the plasmonic crystal system for distances of $d = 0$ and $d = 80$ nm between the building-block arrays. More details can be found in the supporting information.

Supporting Information

Supporting Information is available from the Wiley Online Library or from the author.

Acknowledgements

This work was supported by AFOSR Young Investigator Award FA9550-18-1-0328 and NIST grant 70NANB18H201.

Conflict of Interest

The authors declare no conflict of interest.

Data Availability Statement

Research data are not shared.

Keywords

loading effect, mode hybridization, multiresonant plasmonic devices, nanolaminate plasmonic crystal, spatial mode overlap

Received: November 4, 2020

Revised: January 29, 2021

Published online: March 7, 2021

- [1] J. A. Schuller, E. S. Barnard, W. S. Cai, Y. C. Jun, J. S. White, M. L. Brongersma, *Nat. Mater.* **2010**, *9*, 193.
- [2] L. Novotny, N. van Hulst, *Nat. Photonics* **2011**, *5*, 83.
- [3] A. Kinkhabwala, Z. F. Yu, S. H. Fan, Y. Avlasevich, K. Mullen, W. E. Moerner, *Nat. Photonics* **2009**, *3*, 654.
- [4] J. N. Anker, W. P. Hall, O. Lyandres, N. C. Shah, J. Zhao, R. P. Van Duyne, *Nat. Mater.* **2008**, *7*, 442.
- [5] S. Y. Ding, J. Yi, J. F. Li, B. Ren, D. Y. Wu, R. Panneerselvam, Z. Q. Tian, *Nat. Rev. Mater.* **2016**, *1*, 16021.
- [6] M. L. Brongersma, N. J. Halas, P. Nordlander, *Nat. Nanotechnol.* **2015**, *10*, 25.
- [7] G. Baffou, R. Quidant, F. J. G. de Abajo, *ACS Nano* **2010**, *4*, 709.
- [8] M. Pelton, *Nat. Photonics* **2015**, *9*, 427.
- [9] H. Aouani, M. Navarro-Cia, M. Rahmani, T. P. H. Sidiropoulos, M. Hong, R. F. Oulton, S. A. Maier, *Nano Lett.* **2012**, *12*, 4997.
- [10] M. Kauranen, A. V. Zayats, *Nat. Photonics* **2012**, *6*, 737.
- [11] K. Thyagarajan, J. Butet, O. J. Martin, *Nano Lett.* **2013**, *13*, 1847.
- [12] M. Celebrano, X. F. Wu, M. Baselli, S. Grossmann, P. Biagioni, A. Locatelli, C. De Angelis, G. Cerullo, R. Osellame, B. Hecht, L. Duo, F. Ciccacci, M. Finazzi, *Nat. Nanotechnol.* **2015**, *10*, 412.
- [13] K. T. Lee, J. H. Park, S. J. Kwon, H. K. Kwon, J. Kyhm, K. W. Kwak, H. S. Jang, S. Y. Kim, J. S. Han, S. H. Lee, D. H. Shin, H. Ko, I. K. Han, B. K. Ju, S. H. Kwon, D. H. Ko, *Nano Lett.* **2015**, *15*, 2491.
- [14] Y. Zhang, A. Manjavacas, N. J. Hogan, L. Zhou, C. Ayala-Orozco, L. Dong, J. K. Day, P. Nordlander, N. J. Halas, *Nano Lett.* **2016**, *16*, 3373.
- [15] S. D. Gennaro, Y. Li, S. A. Maier, R. F. Oulton, *ACS Photonics* **2018**, *5*, 3166.
- [16] L. Bonacina, P. F. Brevet, M. Finazzi, M. Celebrano, *J. Appl. Phys.* **2020**, *127*, 230901.
- [17] P. Dombi, Z. Papa, J. Vogelsang, S. V. Yalunin, M. Sivis, G. Herink, S. Schafer, P. Gross, C. Ropers, C. Lienau, *Rev. Mod. Phys.* **2020**, *92*, 025003.
- [18] Q. X. Shen, W. L. Jin, G. Yang, A. W. Rodriguez, M. H. Mikkelsen, *ACS Photonics* **2020**, *7*, 901.
- [19] C. L. You, A. C. Nellikka, I. De Leon, O. S. Magana-Loaiza, *Nanophotonics* **2020**, *9*, 1243.
- [20] S. A. S. Tali, W. Zhou, *Nanophotonics* **2019**, *8*, 1199.
- [21] E. Prodan, C. Radloff, N. J. Halas, P. Nordlander, *Science* **2003**, *302*, 419.
- [22] H. Wang, D. W. Brandl, P. Nordlander, N. J. Halas, *Acc. Chem. Res.* **2007**, *40*, 53.
- [23] M. Hentschel, M. Saliba, R. Vogelgesang, H. Giessen, A. P. Alivisatos, N. Liu, *Nano Lett.* **2010**, *10*, 2721.
- [24] A. E. Cetin, H. Altug, *ACS Nano* **2012**, *6*, 9989.
- [25] H. Harutyunyan, G. Volpe, R. Quidant, L. Novotny, *Phys. Rev. Lett.* **2012**, *108*, 217403.
- [26] K. Thyagarajan, S. Rivier, A. Lovera, O. J. F. Martin, *Opt. Express* **2012**, *20*, 12860.
- [27] S. D. Liu, E. S. P. Leong, G. C. Li, Y. Hou, J. Deng, J. H. Teng, H. C. Ong, D. Y. Lei, *ACS Nano* **2016**, *10*, 1442.
- [28] H. Wang, D. W. Brandl, F. Le, P. Nordlander, N. J. Halas, *Nano Lett.* **2006**, *6*, 827.
- [29] R. Bardhan, S. Mukherjee, N. A. Mirin, S. D. Levit, P. Nordlander, N. J. Halas, *J. Phys. Chem. C* **2010**, *114*, 7378.
- [30] S. Mukherjee, H. Sobhani, J. B. Lassiter, R. Bardhan, P. Nordlander, N. J. Halas, *Nano Lett.* **2010**, *10*, 2694.
- [31] C. Ayala-Orozco, J. G. Liu, M. W. Knight, Y. M. Wang, J. K. Day, P. Nordlander, N. J. Halas, *Nano Lett.* **2014**, *14*, 2926.
- [32] S. Hong, J. A. I. Acapulco, H. Y. Jang, S. Park, *Chem. Mater.* **2014**, *26*, 3618.
- [33] L. Wollet, B. Frank, M. Schaferling, M. Mesch, S. Hein, H. Giessen, *Opt. Mater. Express* **2012**, *2*, 1384.
- [34] W. Zhou, J. Y. Suh, Y. Hua, T. W. Odom, *J. Phys. Chem. C* **2013**, *117*, 2541.
- [35] J. Song, W. Zhou, *Nano Lett.* **2018**, *18*, 4409.
- [36] S. A. S. Tali, W. Zhou, presented at "Multi-resonant Optical Nanocavities by Out-of-Plane Magnetic Plasmon Hybridization", Washington, DC, September **2018**.
- [37] N. Maccaferri, Y. Q. Zhao, T. Isoniemi, M. Iarossi, A. Parracino, G. Strangi, F. De Angelis, *Nano Lett.* **2019**, *19*, 1851.
- [38] O. Reshef, M. Saad-Bin-Alam, M. J. Huttunen, G. Carlow, B. T. Sullivan, J.-M. Ménard, K. Dolgaleva, R. W. Boyd, *Nano Lett.* **2019**, *19*, 6429.
- [39] R. Alaei, M. Albooyeh, C. Rockstuhl, *J. Phys. D: Appl. Phys.* **2017**, *50*, 503002.
- [40] R. Alaei, M. Albooyeh, M. Yazdi, N. Komjani, C. Simovski, F. Lederer, C. Rockstuhl, *Phys. Rev. B* **2015**, *91*, 115119.
- [41] C. Genet, T. W. Ebbesen, in *Nanoscience and Technology: A Collection of Reviews from Nature Journals* (Ed: P. Rodgers), World Scientific, Singapore **2010**, p. 205.
- [42] N. Liu, L. Fu, S. Kaiser, H. Schweizer, H. Giessen, *Adv. Mater.* **2008**, *20*, 3859.
- [43] E. D. Palik, *Handbook of Optical Constants of Solids*, Academic Press, Cambridge, MA, USA **1998**.